Lattice Boltzmann modeling of pool boiling with large liquid-gas density ratio

Wen-Zhen Fang [a], Li Chen [a], Qin-Jun Kang [b], Wen-Quan Tao [a, *]

[a] Key Laboratory of Thermo-Fluid Science and Engineering, MOE, Xi'an Jiaotong University, Xi'an, China
[b] Computational Earth Science Group (EES-16), Los Alamos National Laboratory, Los Alamos, NM, USA

ABSTRACT

In the present paper, a 2D multiple-relaxation-time pseudopotential lattice Boltzmann model combined with the modified thermal lattice Boltzmann method is adopted to simulate the bubble nucleation, growth and departures process on a heated plate. It is a direct numerical simulation of boiling heat transfer determined by the local temperature and thermodynamic relation given by the equation of state. By using a smaller value of a in the P-R equation of state, a thicker liquid-vapor interface is formed and a better numerical stability at a large liquid/vapor density ratio is obtained. Furthermore, the conjugated boundary of heated plate and fluids is specially dealt with to avoid the rapid change of heat flux at the interface. The boiling heat transfer at a density ratio around 200 can be simulated. The results show that: the boiling heat flux decreases during the bubble expansion process while increases during the rewetting process; the average heat flux of boiling at $T_s = 0.68T_c$ is much larger than that at $T_s = 0.86T_c$; bubble occurs earlier on a hydrophobic surface than a hydrophilic one; there exists a remained vapor on a hydrophobic surface after bubble departure, while it is not observed for hydrophilic surface; for the simulated boiling curve, the maximum (critical) heat flux decreases with the decreasing wettability of surfaces; there exists an optimal width of the rectangular cavity making the best heat transfer performance of surfaces; in this study, the roughness surface with a circle cavity has the best heat transfer performance.

© 2016 Elsevier Masson SAS. All rights reserved.

1. Introduction

Boiling heat transfer has been widely studied because of its high heat transfer coefficient and wide applications in many heat-exchange devices [1—3]. At the boiling heat transfer curve [4,5], nucleate boiling is the basic regime characterizing fundamental features of the boiling heat transfer. Although many experimental works have been conducted to study the nucleate boiling, its mechanism and heat transfer characteristics are still not understood completely. With the rapid development of the computer, numerical method has been an attractive and effective method to investigate boiling heat transfer. Son and Dhir [6] first proposed a Level-Set method to capture liquid-vapor interface during boiling process. Subsequently, Welch and Wilson [7] developed the volume of fluid (VOF) method to simulate film boiling process. Sun and Tao [8] proposed the VOSET method for capturing liquid-vapor

interface which possesses advantages of both Level Set and VOF, and meanwhile can overcome their drawbacks. Then, Ling et al. [9] adopted the VOSET method to study nucleate boiling heat transfer problem. Those methods are all tracking liquid-vapor interface methods, in which an initial bubble nucleus should be assigned at the heating wall and a waiting period between two bubble growth cycles should be assumed. Hence, those interface tracking methods can not be adopted to describe bubble nucleation process and obtain the boiling heat transfer curve.

In recent decades, the lattice Boltzmann method (LBM) has been applied to simulate multiphase flow, in which the pseudopotential LB model receives extensive attention due to its kinetic nature and automatic phase separation via an inter-particle potential [10—12]. The multiphase LBM combined with an energy equation model can be applied to simulate the liquid-vapor phase change heat transfer. For the pseudopotential LB model (without thermal LB model), a density disturbance should be assigned into the system to motivate the automatic phase separation. While as for the liquid-vapor phase change heat transfer, a pseudopotential LB model combined with a thermal LB model can be used to automatically generate the bubble

nucleation by adding a temperature disturbance [11]. It is because the temperature disturbance will result in a density disturbance in the computational domain through the equation of state. A non-uniform wall temperature or non-uniform structure of the heated plate (with cavities) can be applied at the bottom of computational domain to bring a temperature disturbance into the system, and further to generate the bubble nucleation. It is a direct simulation of phase change heat transfer which is determined by the local temperature and thermodynamic relation given by equation of state. Hazi and Markus [13] first proposed a LB model to investigate the heterogeneous boiling on a heating wall by assigning a non-uniform wall temperature. And then Markus and Hazi [14] adopted the LB model to investigate the boiling process on the heated plate with cavities. Recently, Gong and Cheng [15] further developed a single-relaxation-time LB model to simulate liquid-vapor phase change heat transfer, and they adopted this method to investigate influences of the surface wettability and cavities on boiling process [16–18]. Li et al. [19] adopted a hybrid thermal LB model to simulate boiling process by using finite difference method to solve the energy equation and pseudopotential LB model to solve multiphase flow. Generally speaking, in the above studies, three aspects need further improvements. First, the term ρc_v in the energy equation is often taken as constant and put into $\nabla \cdot (\lambda \nabla T)$ to obtain term $\nabla \cdot (a \nabla T)$, which will bring heat flux discontinuity at the grid interface for the thermal LBM [20]. Second, the conjugated boundary at the interface of the heated plate and fluids is not appropriately treated for the thermal LBM, which will bring a major heat flux discontinuity at this interface [20]. Third, the density ratio (liquid versus vapor) is quite limited (usually less than 20). It is mainly because the pseudopotential LB model suffers thermodynamic inconsistency and large spurious currents [11,21], and the single-relaxation-time LB model also has some limitations in this regard. In recent years, it has been found that the multiple-relaxation-time (MRT) LBM has much better numerical stability than the single-relaxation-time LBM [22].

In the present study, we adopt the MRT pseudopotential LBM proposed by Li et al. [22] combined with a modified thermal LBM to simulate the boiling nucleation, growth and departure process on a heated plate with a special treatment at conjugated boundary (interface of the heated plate and fluids). The MRT pseudopotential LBM proposed by Li et al. [22] can approximately achieve thermodynamic consistency, which allows us to simulate multiphase flow at a larger density ratio. The developed liquid-vapor phase change heat transfer model can simulate boiling nucleation process at a saturation temperature as low as 0.68 T_c, with density ratio around 200:1 and the kinematic viscosity ratio around 1:20 (liquid versus vapor). As indicated above, some artificial disturbances (say, by setting a higher temperature at the heating surface) were often needed to stimulate the generation of a vapor embryo in the early studies. We believe that any non-uniformity, either in density, temperature or surface structure, all can be considered as a kind of disturbance. In our simulations, surface structures are regarded as the disturbance to generate a vapor embryo, and hence no any other artificial disturbance is needed.

The rest of this paper is organized as follows. Section 2 introduces the MRT pseudopotential LB model and energy equation of the phase-change thermal LB model; Section 3 presents the major numerical results, including discussions of bubble departure diameter and frequency (Section 3.1), vapor bubble growth and heat flux (Section 3.2), comparison of boiling at different saturation temperatures (Section 3.3), influences of the surface wettability on boiling curve (Section 3.4), and influences of cavities on boiling heat transfer (Section 3.5). Finally, some conclusions are made in Section 4.

2. Numerical method

2.1. MRT pseudopotential lattice Boltzmann method

In this paper, a MRT LBM is adopted to solve multiphase flow. We consider a D2Q9 LB model with a multiple-relaxation-time collision operator [23]:

$$f_i(\boldsymbol{x} + \boldsymbol{e}_i \delta_t, t + \delta_t) - f_i(\boldsymbol{x}, t) = -\left(\mathbf{M}^{-1}\mathbf{SM}\right)_{ij}\left[f_j - f_j^{eq}\right] + \delta_t F_i \quad (1)$$

where $\mathbf{M}$ is an orthogonal transformation matrix, defined as:

$$\mathbf{M} = \begin{bmatrix} 1, & 1, & 1, & 1, & 1, & 1, & 1, & 1, & 1 \\ -4, & -1, & -1, & -1, & -1, & 2, & 2, & 2, & 2 \\ 4, & -2, & -2, & -2, & -2, & 1, & 1, & 1, & 1 \\ 0, & 1, & 0, & -1, & 0, & 1, & -1, & -1, & 1 \\ 0, & -2, & 0, & 2, & 0, & 1, & -1, & -1, & 1 \\ 0, & 0, & 1, & 0, & -1, & 1, & 1, & -1, & -1 \\ 0, & 0, & -2, & 0, & 2, & 1, & 1, & -1, & -1 \\ 0, & 1, & -1, & 1, & -1, & 0, & 0, & 0, & 0 \\ 0, & 0, & 0, & 0, & 0, & 1, & -1, & 1, & -1 \end{bmatrix} \quad (2)$$

$\mathbf{S}$ is a diagonal matrix:

$$\mathbf{S} = \mathrm{diag}\left(\tau_\rho^{-1}, \tau_e^{-1}, \tau_\varsigma^{-1}, \tau_j^{-1}, \tau_q^{-1}, \tau_j^{-1}, \tau_v^{-1}, \tau_v^{-1}\right) \quad (3)$$

and F_i is the force term, given by Ref. [23]:

$$\mathbf{F} = \mathbf{M}^{-1}\left(\mathbf{I} - \frac{1}{2}\mathbf{S}\right)\mathbf{M}\bar{\mathbf{F}} \quad (4)$$

where $\mathbf{F} = (F_0, F_1, ..., F_8)^\mathrm{T}$; $\mathbf{I}$ is the unit tensor; and $\bar{\mathbf{F}} = (\bar{F}_0, \bar{F}_1, ..., \bar{F}_8)^\mathrm{T}$ with

$$\bar{F}_i = \omega_i\left[\frac{\boldsymbol{e}_i \cdot \mathbf{F}}{c_s^2} + \frac{\mathbf{uF} : (\boldsymbol{e}_i\boldsymbol{e}_i - c_s^2\mathbf{I})}{2c_s^4}\right] \quad (5)$$

The macroscopic density and physical velocity can be obtained by Ref. [22]:

$$\rho = \sum_i f_i \quad (6)$$

$$\rho\mathbf{u} = \sum_i \boldsymbol{e}_i f_i + \frac{\delta_t}{2}\mathbf{F} \quad (7)$$

where $\mathbf{F} = (F_x, F_y)$ is the total force acting on the fluid particle, which includes fluid-fluid molecular interaction force $\mathbf{F}_f$, fluid-solid interaction force $\mathbf{F}_s$ and body force $\mathbf{F}_b$. Usually, the force term is incorporated into the MRT LB model with the following scheme [24].

$$\mathbf{F}_\mathrm{m} = \mathbf{M}\bar{\mathbf{F}} = \begin{bmatrix} 0 \\ 6\mathbf{uF} \\ -6\mathbf{uF} \\ F_x \\ -F_x \\ F_y \\ -F_y \\ 2(uF_x - vF_y) \\ (uF_y + vF_x) \end{bmatrix} \quad (8)$$

where $\mathbf{F}_\mathrm{m}$ is the force term in the moment space, but such force scheme suffers thermodynamic inconsistency. An improved force scheme was proposed by Li et al. [22] to approximately achieve

thermodynamic consistency:

$$\mathbf{F}'_m = \begin{bmatrix} 0 \\ 6\mathbf{uF} + \dfrac{12\sigma\left|\mathbf{F}_f\right|^2}{\psi^2\delta_t(\tau_e - 0.5)} \\ -6\mathbf{uF} + \dfrac{12\sigma\left|\mathbf{F}_f\right|^2}{\psi^2\delta_t(\tau_e - 0.5)} \\ F_x \\ F_x \\ F_y \\ -F_y \\ 2\left(uF_x - vF_y\right) \\ \left(uF_y + vF_x\right) \end{bmatrix} \tag{9}$$

where σ is a parameter that can be used to tune the mechanical stability condition to achieve thermodynamic consistency. Through numerical test of the two-dimensional circular suspension droplet, we find that the numerical results of $\sigma = 0.107$ agree well with the solution of Maxwell solutions (shown in Fig. 1).

Because of the thermodynamic inconsistency of Eq. (8), simulation results will diverge when saturation temperature is below $0.85T_c$. In contrast, the saturation temperature can be as low as 0.53 T_c if we adopt the force scheme of Eq. (14). $\left|\mathbf{F}_f\right|^2 = (F_{f,x}^2 + F_{f,y}^2)$, in which $\mathbf{F}_f$ is the fluid-fluid molecular interaction force, and can be obtained by Refs. [11,22]:

$$\mathbf{F}_f = -G\psi(\mathbf{x})\sum_i w\left(|\mathbf{e}_i|^2\right)\psi(\mathbf{x}+\mathbf{e}_i)\mathbf{e}_i \tag{10}$$

where G is the interaction strength; $w(|\mathbf{e}_i|^2)$ is the weight; ψ is the pseudopotential, defined as [11,22]:

$$\psi(\mathbf{x})\sqrt{2\left(p_{EOS} - \rho c_s^2\right)}\Big/Gc^2 \tag{11}$$

where p_{EOS} is the non-ideal equation of state. In the present paper, the Peng-Robinson equation of state is adopted [25]:
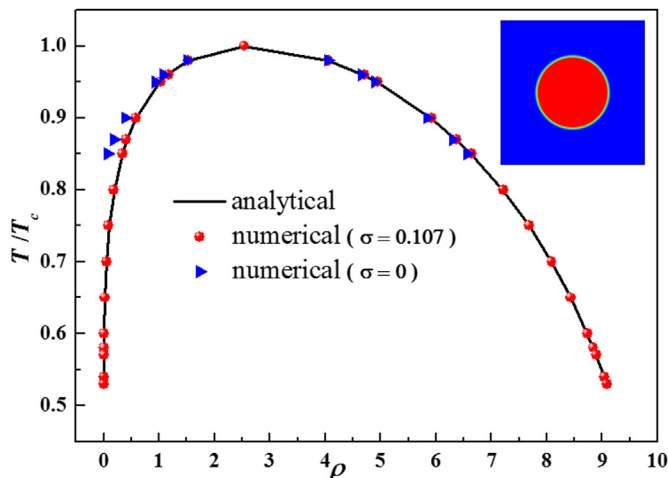
Fig. 1. Coexistence curves.

$$p_{EOS} = \frac{\rho RT}{1 - b\rho} - \frac{a\varphi(T)\rho^2}{1 + 2b\rho - b^2\rho^2}$$

$$\varphi(T) = \left[1 + \left(0.37464 + 1.54226\omega - 0.26992\omega^2\right)\left(1 - \sqrt{T/T_c}\right)\right]^2 \tag{12}$$

where $a = 0.45724R^2T_c^2/p_c$ and $b = 0.0778RT_c/p_c$. In the present paper, $b = 2/21$, $\omega = 0.344$, $R = 1$. The pseudopotential LBM is a diffuse interface method, and the width of interfaces always has several lattices. The value of a is related to the width of interface [22]. Table 1 shows influences of a on the interface thickness. A smaller a will result in a thicker interface and a smaller spurious current. The rapid change of physical properties at the interface can be smoothed by a thicker interface, which allow us to simulate multiphase flow at a larger density ratio. The lowest saturation temperature that can be simulated is 0.70 T_c with a density ratio of 145.24 for $a = 0.06122$, while it can be as low as 0.53 T_c with a density ratio of 4560.28 for $a = 0.02267$. In the present paper, we choose $a = 0.02267$ to simulate the pool boiling process.

The fluid-solid interaction force (adhesive force between solid and fluid) can be calculated by Refs. [19,26]:

$$\mathbf{F}_s = -G_w\psi(\mathbf{x})\sum_i w\left(|\mathbf{e}_i|^2\right)\psi(\mathbf{x})s(\mathbf{x}+\mathbf{e}_i)\mathbf{e}_i \tag{13}$$

where s is the indicator function which equals 0 for fluids and equals 1 for solids; G_w is used to tune the wettability (contact angle) of surfaces.

The gravitational force can be calculated by Ref. [11]:

$$\mathbf{F}_b = (\rho - \rho_{ave})\mathbf{g} \tag{14}$$

where ρ_{ave} is the average density of computational domain; $\mathbf{g} = (0, -g)$ is the gravitational acceleration.

At the liquid-vapor interface, the viscosity is smoothed by:

$$v = v_l\frac{\rho - \rho_v}{\rho_l - \rho_v} + v_v\frac{\rho_l - \rho}{\rho_l - \rho_v} \tag{15}$$

where subscripts l and v represent liquid and vapor, respectively. The relation between the viscosity and relation time coefficient is:

$$v = c_s^2(\tau_v - 0.5)\delta t \tag{16}$$

In the present paper, after a number of preliminary computations, following values for relaxation time coefficients are obtained: $\tau_\rho = \tau_j = 1.0$, $\tau_e = \tau_\varsigma = 1.2$, $\tau_q = 1.1$, while τ_v is determined by the local property.

2.2. Energy equation of the phase-change thermal LB model

By neglecting the viscous dissipation, the entropy balance equation yields [15]:

$$\rho T\frac{ds}{dt} = \nabla.(\lambda\nabla T) \tag{17}$$

Table 1
The influence of a on the interface thickness.

	Thickness (lattice)	Lowest temperature (T/T_c)	Density ratio
$a = 0.06122$	5.72	0.70	145.24
$a = 0.04082$	5.94	0.63	471.88
$a = 0.02267$	7.37	0.53	4560.28

where s is the entropy; and λ is the thermal conductivity. According to the thermodynamic relation of entropy, we have [15]:

$$Tds = c_v dT + T\left(\frac{\partial p_{EOS}}{\partial T}\right)d\left(\frac{1}{\rho}\right) \tag{18}$$

Substituting Eq. (18) to Eq. (17) yields:

$$\rho c_v \frac{dT}{dt}\nabla.(\lambda\nabla T) - T\left(\frac{\partial p_{EOS}}{\partial T}\right)\nabla\cdot\mathbf{u} \tag{19}$$

In the present paper, we adopt MRT LBM to solve the energy equation [15]:

$$h_i(\mathbf{x} + \mathbf{e}_i\delta_t,\ \ t + \delta_t) - h_i(\mathbf{x},\ \ t) = -\left(\mathbf{M}^{-1}\mathbf{S}_T\mathbf{M}\right)_{ij}\left[h_j - h_j^{eq}\right] + \delta_t\omega_i\phi \tag{20}$$

with

$$\mathbf{S}_T = \text{diag}\left(\tau_0^{-1},\ \ \tau_1^{-1},\ \ \tau_2^{-1}, \tau_T^{-1},\ \ \tau_4^{-1},\ \ \tau_T^{-1},\ \ \tau_6^{-1},\ \ \tau_7^{-1},\ \ \tau_8^{-1}\right) \tag{21}$$

where τ_T is the relaxation time related to the thermal diffusivity:

$$a = c_s^2(\tau_T - 0.5)\delta t \tag{22}$$

This LB model can retrieve the following advection-diffusion energy equation by using the Chapman-Enskog expansion [20]:

$$\frac{\partial T}{\partial t} + \nabla.(\mathbf{u}T) = \nabla\cdot(a\nabla T) + \phi \tag{23}$$

where ϕ is the source term. Eq. (19) can be rewritten as:

$$\frac{\partial T}{\partial t} + \nabla.(\mathbf{u}T) = \nabla\cdot(a\nabla T) - \nabla\left(\frac{1}{\rho c_v}\right)\cdot(\lambda\nabla T) + T\left[1 - \frac{1}{\rho c_v}\left(\frac{\partial p_{EOS}}{\partial T}\right)\right] \times \nabla\cdot\mathbf{u} \tag{24}$$

where the second term on the right side of Eq. (24) is the source term due to the spatially variable ρc_v in the computational domain, which is neglected in References [15–18]; the third term is the source term responsible for the phase change.

2.3. Boundary conditions

Numerical simulations are conducted in a 2D computational domain with a 200 × 600 grid system. Two kinds of heated plates are placed at the center of the computational domain, as shown in Fig. 2. The computational domains of Fig. 2(a) and Fig. 2(b) are used to study influences of surface wettability and cavity on the boiling process, respectively. The boundary conditions are shown in Fig. 2(a): the periodic boundary is applied at the left and right sides of computational domain; the convective boundary condition is applied at the top of computational domain; the adiabatic boundary condition is applied at the left and right sides of the heated plate; the constant temperature is applied at the bottom side of the heated plate. For the details of boundary treatments in LBM, one can refer to references [27–29].

Note that the top side of heated plate is the conjugated boundary condition in that both the temperature in fluids and solid should be simultaneously solved, rather than pre-specified the top side temperature [30]. Such a conjugated boundary should be carefully treated to ensure the continuity of temperature and heat flux at the boundary. With the half lattice treatment, the temperature distribution function at conjugated boundary can be expressed as [31]:

$$h_{\bar{i}}\left(\mathbf{x}_f, t + \delta t\right) = \frac{1 - \beta}{1 + \beta}h_i^*\left(\mathbf{x}_f, t\right) + \frac{2\beta}{1 + \beta}h_{\bar{i}}^*(\mathbf{x}_s, t)$$
$$h_i(\mathbf{x}_s, t + \delta t) = \frac{1 - \beta}{1 + \beta}h_{\bar{i}}^*(\mathbf{x}_s, t) + \frac{2}{1 + \beta}h_i^*\left(\mathbf{x}_f, t\right) \tag{25}$$

where $\mathbf{x}_s$ denotes the node at the heated plate; $\mathbf{x}_f$ denotes the node at the flow region; $\bar{i}$ denotes the opposite direction of i; and $\beta = (\rho c_v)_s/(\rho c_v)_f$. If $\beta = 1$, Eq. (25) can be reduced as:

$$h_{\bar{i}}\left(\mathbf{x}_f, t + \delta t\right) = h_{\bar{i}}^*(\mathbf{x}_s, t)$$
$$h_i(\mathbf{x}_s, t + \delta t) = h_i^*\left(\mathbf{x}_f, t\right) \tag{26}$$

It is the same with the streaming process in LBM, which means that if $\beta = 1$, no additional treatment is needed at the conjugated boundary.

For LBM, the recovered macroscopic energy equation is Eq. (23), and it is the diffusive flux $a\nabla T$ that conserved at the conjugated boundary rather than heat flux. Considering a simple case of pure conduction in a two-component medium, as shown in Fig. 3 (a), heat is conducted from top side to the bottom side through the interface. Suppose there is no contact resistance at the interface, from Eq. (23), we should have $a_1\nabla T = a_2\nabla T$ conserved at the interface rather than $\lambda_1\nabla T = \lambda_2\nabla T$. But physically it is the heat flux continued at the interface, and thus additional treatment is needed at the interface as shown by Eq. (25). As shown in Fig. 3 (b), with such a special treatment, the temperature distribution agrees well with the analytical result. In the present paper, ρv_v of the heated plate is much larger than that of the liquid or vapor, which will lead to a significant jump of heat flux at the conjugated boundary if no additional treatment at the interface is assigned.

2.4. Validation

In the present paper, we improved the liquid-vapor phase change LB model. To validate the present model, a benchmark concerning evaporation is conducted [16]. The schematic of computational domain and boundary conditions are shown in Fig. 4 (a). The liquid evaporates into vapor at the interface by absorbing heat from the bottom at the saturation temperature of $0.86T_c$. The input heat flux should be small enough to avoid boiling at the internal of liquid. For a certain heat flux, the stable stream mass flow rate can be obtained by:

$$q = m\prime h_{fg} \tag{27}$$

where h_{fg} is the latent heat. The predicted stream mass flow rates with the input heat flux are presented in Fig. 4(b), which agrees well with analytical results.

3. Results and discussion

3.1. Bubble departure diameter and release frequency

Many studies have been conducted to investigate the bubble departure diameter and bubble release frequency [13,15]. From the static force balance of adhesive force and buoyant force, the following relation between the bubble diameter and gravity was derived by Fritz [32]:

(a) α- model (b) β - model

Fig. 2. Computational domain and boundary conditions.

(a) Schematic of two-component medium (b) Temperature distribution along y direction
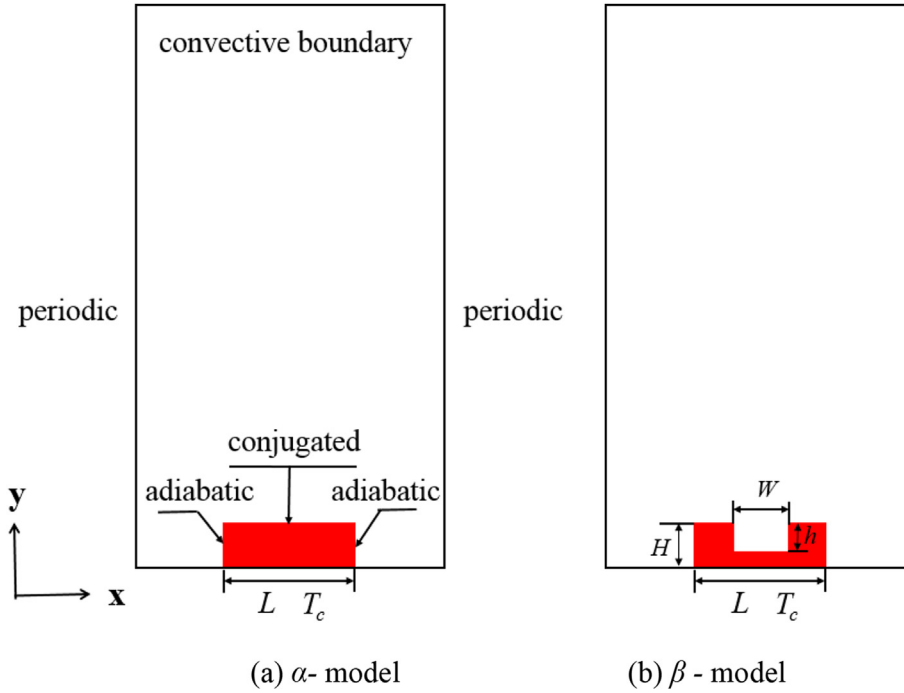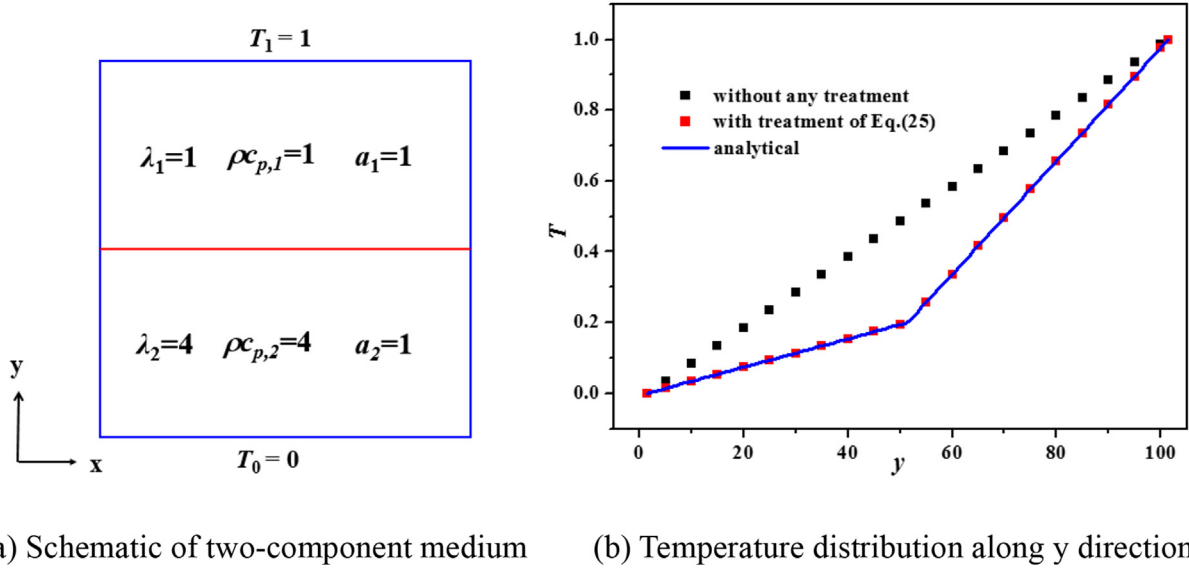
Fig. 3. Comparison of results of different treatments at the interface.

$$D_b \sim \sqrt{\frac{\sigma}{g\left(\rho_l - \rho_g\right)}} \qquad (28)$$

As for the bubble release frequency, the most famous correlation is proposed by Zuber [33]:

$$f^{-1} \sim D_b \left[\frac{\sigma g\left(\rho_l - \rho_g\right)}{\rho_l^2}\right]^{-0.25} \qquad (29)$$

With the fact that the bubble departure diameter is proportional

to $g^{-0.5}$ derived by Fritz, the bubble release frequency is proportional to $g^{-0.75}$.

In this section, the bubble departure diameter and release period as a function of gravity are numerically obtained based on the α-model structure (shown in Fig. 2 (a)). Fig. 5(a) shows the numerical results of bubble departure diameters varying with the gravity force (In this paper, all the physical parameters are in lattice units). The exponent of the fitting curve of our numerical results is −0.514, which agrees well with the correlation given by Fritz [32]. Fig. 5(b) shows the numerical results of bubble release frequency varying with the gravity force. The exponent of the fitting curve of our numerical results is −0.7875, which is a little bigger (absolute

(a) Computational domain   (b) Heat flux . vs. stream mass flow rate (lattice unit)
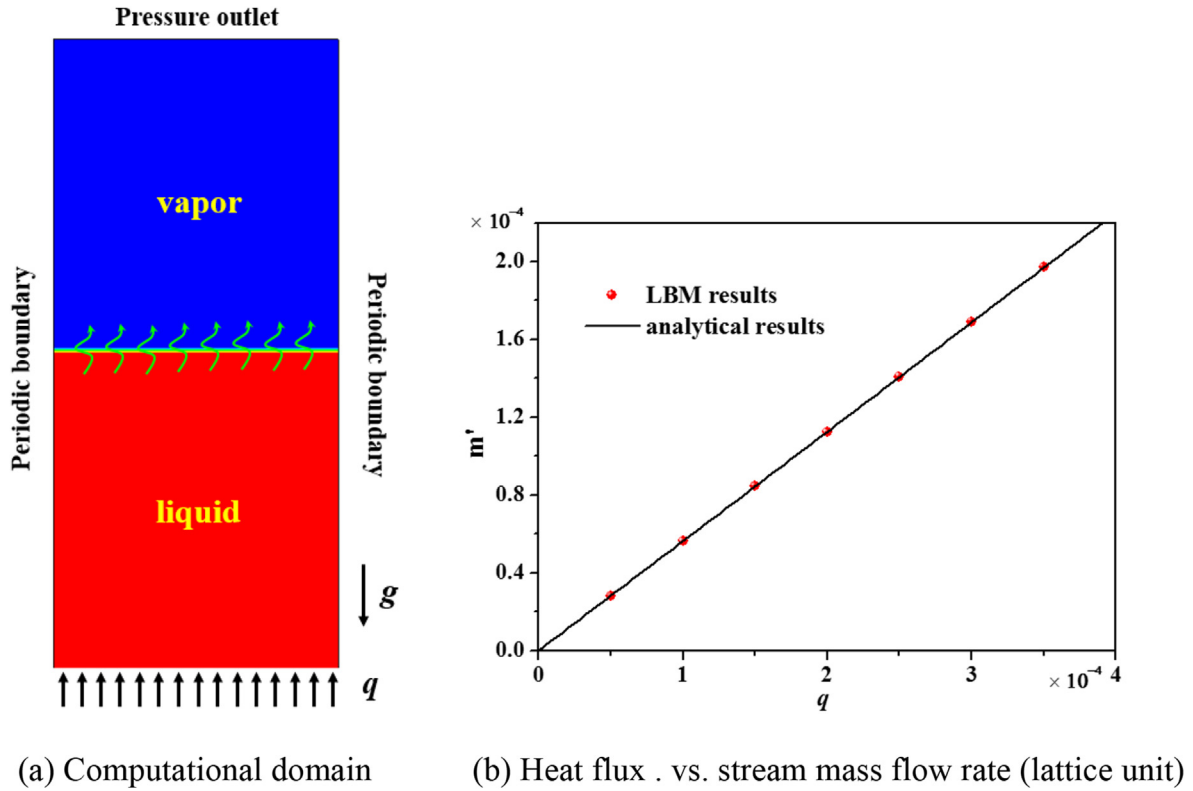
Fig. 4. Model validation of an evaporation case.

(a) Bubble departure diameter   (b) Bubble release frequency
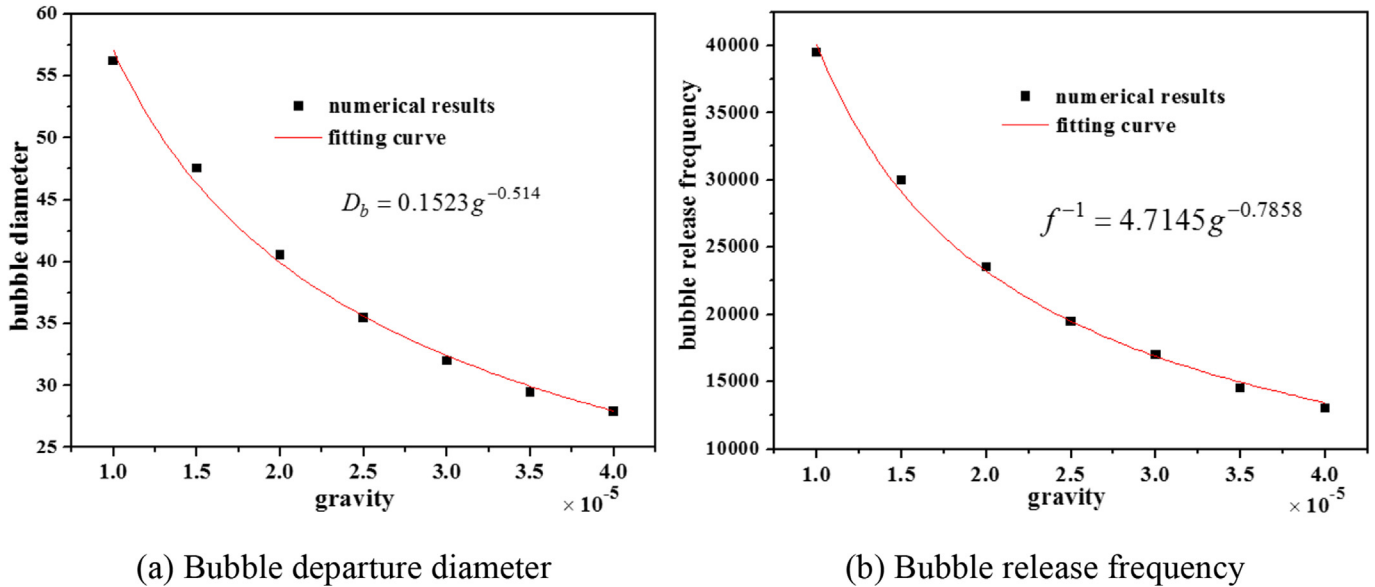
Fig. 5. The influence of gravity.

value) than the analytical results of Zuber [33]. One possible reason for this deviation may result from the fact that natural convection developing between the liquid and heated plate is not considered in the analytical results.

3.2. Vapor bubble growth and heat flux

Three-phase contact line (TCL) means the contact line of vapor,

liquid and solid. Fig. 6 shows the three-phase contact line movement during the vapor bubble growth process. The results are obtained at the static contact angle of 95°, and Jacob number is 0.142 which is defined as follows:

$$Ja = \frac{c_{vl}(T_w - T_s)}{h_{fg}} \qquad (30)$$

(a) Before bubble departure   (b) After bubble departure
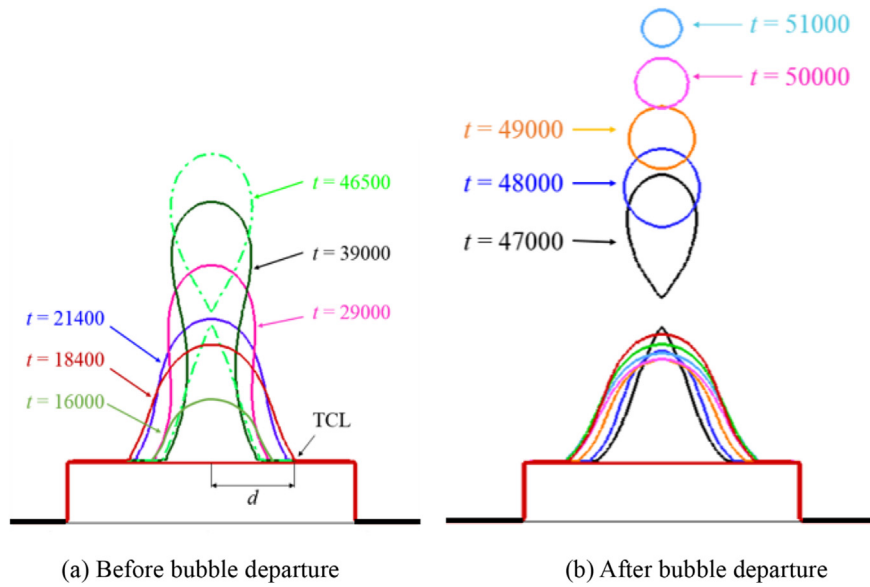
Fig. 6. Vapor bubble growth process.

where T_w and T_s are the wall temperature and saturation temperature, respectively.

As shown in Fig. 6 (a), from $t = 16000$ to $t = 18400$, the three-phase contact line moves outward and the vapor bubble volume increases, which is called as expansion process; after that, the three-phase contact line starts to moves inward, which is called rewetting process. Due to the action of the buoyant force, a vapor neck appears at $t = 29000$, and finally the bubble breaks at $t = 46500$. After bubble departure, the remained part continues to grow and a new bubble growth cycle begins. The dynamic bubble movement after departure is presented in Fig. 6 (b). The volume of the departure bubble gradually decreased during the rise process, which is also observed in the literature [13]. It is because the temperature inside the vapor bubble generated from the bottom is overheated and higher than the surrounding liquid. Therefore, the departure bubble condenses and finally collapses after moving a certain distance. The distance between the three-phase contact line and center, denoted as d, is recorded during the vapor bubble growth process, as shown in Fig. 7. At the minimum value of d, the vapor bubble departs. The first two bubble growth cycles have a longer duration time than the following cycles which are almost periodically repeated.

The local wall heat flux and average wall heat flux of the upper surface of the heated plate can be obtained by:

$$q_w = -\lambda_w \left(\frac{\partial T}{\partial y}\right)_{y=H} \tag{31}$$

$$\bar{q}_w = \int q_w dx / L \tag{32}$$

Fig. 7 also shows average wall heat flux of the upper surface of the heated plate varying with time. As shown, the wall heat flux increases during the rewetting process and reaches the peak at the time of bubble departure (d at minimum value), while decreases during the expansion process and reaches a minimum value when d is at the maximum value. It is because the thermal conductivity of liquid is much larger than that of vapor. Meanwhile, the departure of the bubble brings disturbance into flow field and reduces the thickness of the thermal boundary layer. The local q_w and q_f are shown in Fig. 8. The local heat flux at the first fluid layer adjacent to the heated plate can be obtained by:
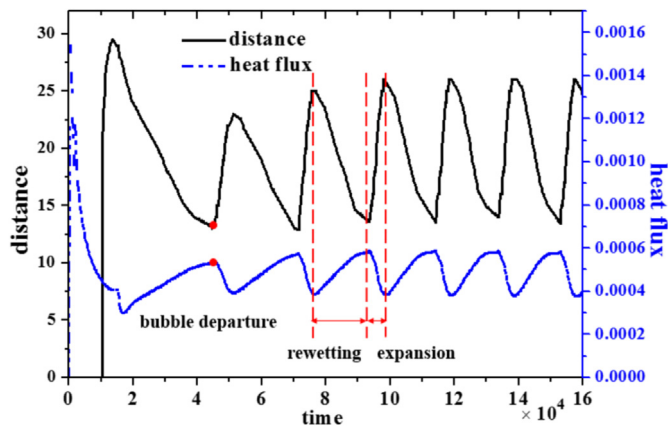
Fig. 7. Three-phase contact line and heat flux vs. time.
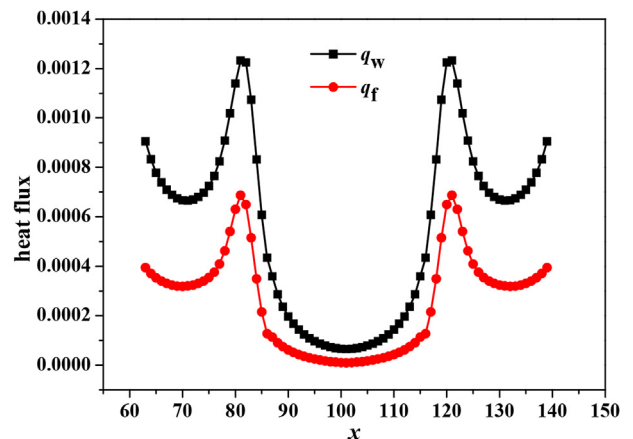
Fig. 8. The local heat flux variation.

$$q_f = -\lambda_f \left(\frac{\partial T}{\partial y} \right)_{y=H+1} \qquad (33)$$

As shown in Fig. 8, the peak value of local heat flux occurs at the position where the three-phase contact point exists. It is because the highest rate of phase change occurs at the three-phase contact point. The local heat flux at the surface covered with the liquid is larger than that at the surface covered with the vapor. The difference of q_w and q_f is due to the source term (including phase change term) of the first fluid layer adjacent to the heated plate. The variation tendencies of q_w and q_f are consistent.

The velocity, density and temperature distributions are shown in Fig. 9. The temperature at the three-phase contact point is lowest due to the highest speed rate of liquid-vapor phase change. The temperature of the surface covered with vapor is higher than that covered with liquid. It is because the thermal conductivity of vapor is much lower than that of liquid. This result agrees with the fact that the bubble occurs at the higher temperature position of the heated surface. In addition, from temperature contours, it can be seen that the temperature inside the bubble is overheated. Therefore, the departure vapor bubble will heat the surrounding liquid until the bubble collapses. It is interested to note that Fig. 9(a) shows a relatively thick interface region. It is because the pseudo-potential LBM is a diffuse interface method, and the width of the interface always has several lattices. A smaller value of a in P-R equation of state leads to a wider thickness interface and a better numerical stability. However, the thickness of interface can be neglected compared with the characteristic length of computational domain. So it will not lead to much inaccuracy of the simulation results.

3.3. Comparison of boiling at different density ratio

In the previous studies, the simulated boiling saturation temperature is 0.86 T_c or 0.9 T_c, and the density, thermal conductivity ratios of the liquid versus vapor are rather low. At $T_s = 0.86T_c$, the density ratio is about 17:1; the kinematic viscosity and thermal diffusivity ratios are about 1:4.3; and the thermal conductivity ratio is about 9:1. In the present study, the simulation saturation temperature can be as low as $T_s = 0.68T_c$. At $T_s = 0.68T_c$, the density ratio is about 200:1; the kinematic viscosity and thermal diffusivity ratios are both about 1:20; and the thermal conductivity ratio is about 20:1. The comparisons of boiling at different saturation

temperatures are shown in Fig. 10 under the same superheat criteria $Ja = 0.142$. Fig. 10(a) shows the diameters of every departed bubble varying with time. It can be seen that the bubble appears earlier at $T_s = 0.86T_c$ than that at $T_s = 0.68T_c$, resulted from the smaller latent heat at $T_s = 0.86T_c$. For each bubble, its diameter reaches the maximum when it is going to depart from the heating surface, and the bubble diameter reduces after bubble departs. At $T_s = 0.68T_c$, the departed bubble collapses before the next bubble departs, while at $T_s = 0.86T_c$, the departed bubble can remain for a longer time. At the same Ja number, the temperature difference, T_w-T_s, at $T_s = 0.86T_c$ is smaller due to the smaller latent heat than that at $T_s = 0.68T_c$. The condensation trend of the departed bubble is stronger at a bigger temperature difference of vapor bubble and surrounding liquid. After the liquid is heated for a certain time, the eighth departure bubble departs before the seventh bubble disappears at $T_s = 0.86T_c$. It means that two bubble coexist at the computational domain, which is not observed at $T_s = 0.68T_c$. Fig. 10(b) shows the comparisons of wall heat flux varying with time at different boiling saturation temperature. Both amplitudes of wall heat flux and average wall heat flux at $T_s = 0.68T_c$ are much larger than those at $T_s = 0.86T_c$ due to the larger latent heat and larger thermal conductivity of the liquid at $T_s = 0.68T_c$.

3.4. Influence of surface wettability

The value of fluid-solid interaction force (adhesive force) can be adjusted by tuning G_w. The variation of the static contact angle of liquid droplet with G_w is shown in Fig. 11. For hydrophilic surface, the static contact angle of droplet is smaller than 90°, while for hydrophobic surface, the contact angle of droplet is larger than 90°.

Fig. 12(a) and Fig. 12(b) show the bubble growth process with the static contact angle of 38.2° and 123.3°, respectively. It can be seen that there is no remained vapor on the surface when the bubble departs with the contact angle of 38.2°, and therefore a nucleation waiting time is needed to generate a new bubble. As for the case of static contact angle of 123.3°, there is a remained part of vapor at the surface when the bubble departs. The remained part of the vapor becomes the nucleus of the next bubble and no nucleation waiting time is needed to generate a new bubble, which is also observed in the experimental work [34].

Fig. 13 shows the average temperature of the upper surface of the heated plate varying with time. From this curve, we can determine the nucleation temperature occurring at the instant of time a when the bubble nucleus generates. At time a, the

(a) Density and velocity vector (b) Temperature

Fig. 9. The velocity, density and temperature distributions.

(a) Bubble diameter .vs. time

(b) Heat flux .vs. time
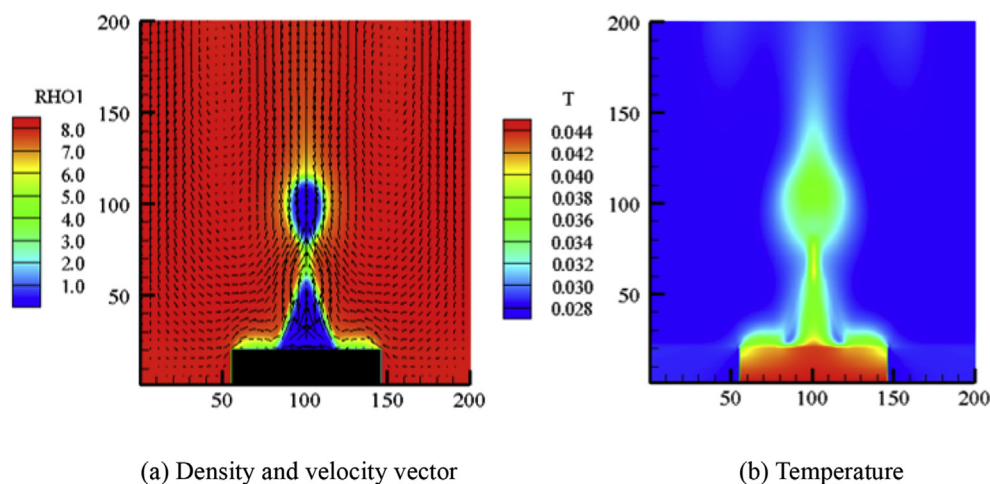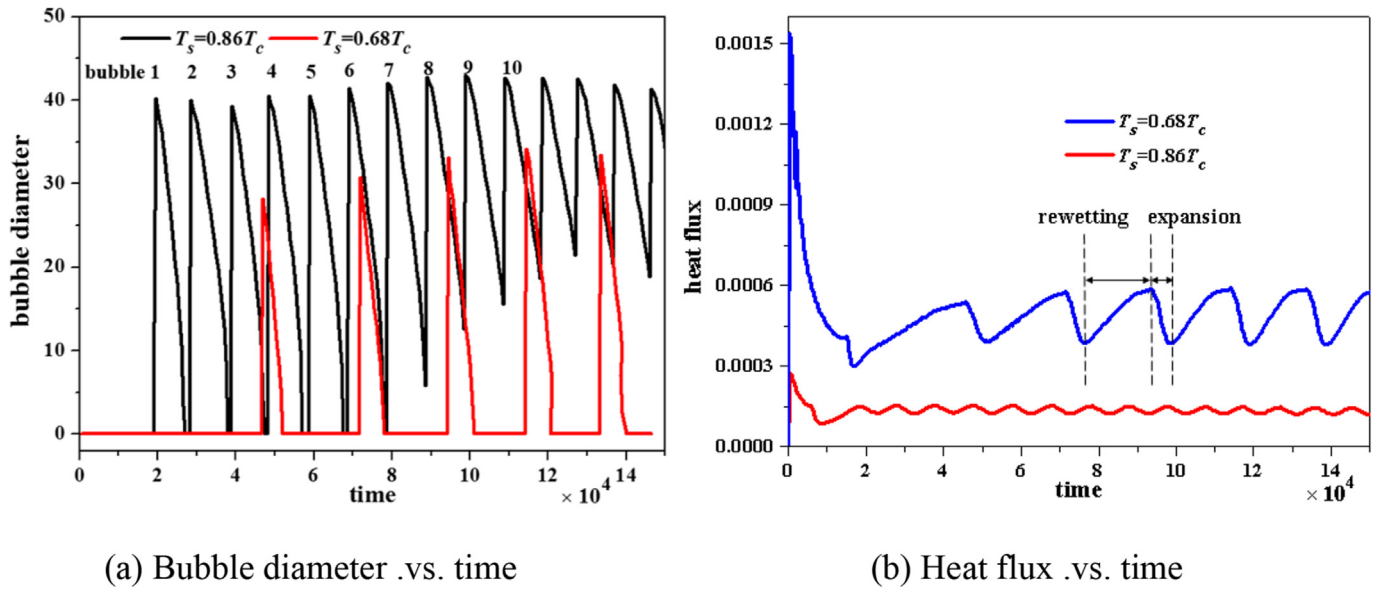
Fig. 10. Comparisons of boiling at different saturation temperatures.
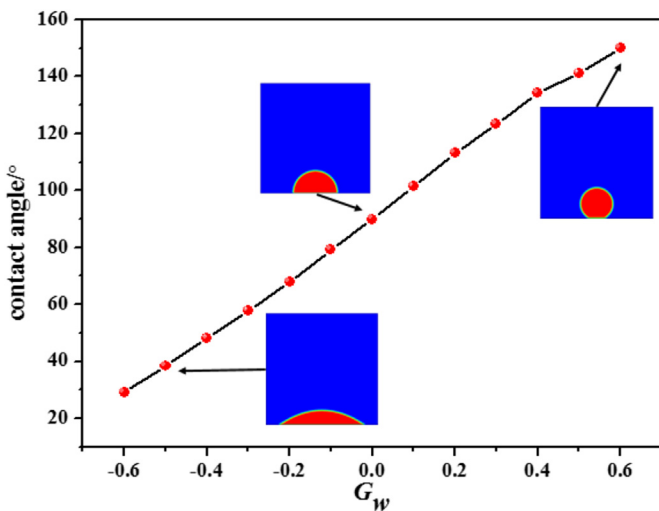
Fig. 11. The variation of contact angle with G_w.

temperature significantly rises due to the small thermal conductivity of the vapor. From the instant of time a to time b, the average temperature of the surface rises due to the bubble at the expansion stage; while from time b to time c, the average wall temperature of the upper surface decreases due to the bubble at the rewetting stage. This time variation of wall temperature is confirmed by Myers et al. [35] at their experimental work. Table 2 presents the nucleation waiting time of first bubble (the first bubble nucleus occurs) varying with the static contact angle. As shown, the nucleation waiting time of first bubble decreases with the decreasing surface wettability. It means that the bubble occurs earlier on a hydrophobic surface than a hydrophilic surface, which is also observed by Jo et al. [34] at their experimental work.

A small size of the heated plate is used to study the generation process of a single bubble. However, to investigate the effect of surface wettability on the boiling curve, a larger size of heated plate has to be adopted where many vapor embryos can be formed. Fig. 14 shows the boiling curves at the static contact angle of 52.9°,

62.8°, 73.5°, respectively. The heat flux first increases with the superheat and then decreases. Taking the static contact angle of 52.9° as an example, the boiling is at the nucleate boiling stage from $Ja = 0.111$ to $Ja = 0.227$ (Fig. 14), and then it goes into the transition boiling stage. Correspondingly, the heat flux increases with the superheat, reaching the maximum heat flux at $Ja = 0.227$, and then decreases. It can be observed that the maximum (critical) heat flux decreases when the static contact angle increases, which agrees with the trend revealed in literature [36]. At the very low superheat region, the heat flux increases with the static contact angle. This is due to the fact that the bubble occurs earlier on surfaces with a larger contact angle (shown in Table 2). However, the vapor bubble trends to be more likely to expand along the surface with a larger contact angle, which will lead to a smaller maximum heat flux occurred at a lower superheat Ja number. This phenomenon is also reported in literature [19].

3.5. Influence of cavity

In this section, the influence of cavity at the surface of the heated plate on the wall heat flux is investigated. Hereafter, the value of G_w is set to be 0, which means the surface is neutral. The heat flux of the surface with cavity is recorded at the bottom of heated plate.

3.5.1. Influence of rectangular cavity width

The influence of the rectangular cavity width on the bubble growth process and wall heat flux is investigated (see β-model structure in Fig. 2(b)). The height H and length L of the heated plate are 20 and 90 (lattice unit), respectively. The depth of the rectangular, h, remains 15, while the width of rectangular cavity, W, is changing from 10 to 50. Comparisons of the heat transfer performance of the surface with different cavity widths are shown in Fig. 15 (a). The zero rectangular width represents no cavity at the upper surface of the heated plate, and its wall heat flux is the reference line. The average heat flux first increases with the width of the cavity and then decreases, reaching a peak at the width of the cavity being 30. The average heat flux of the surface with cavity width being 30 is 89% higher than that of the surface without cavity. It can also be seen that the bubble release frequency first increases with the cavity width and then approaches a certain value. The
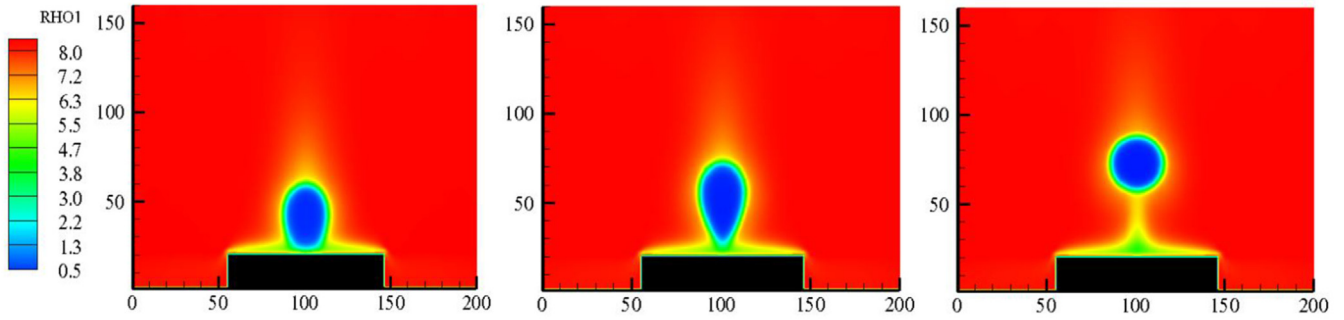
(a) Static contact angle of 38.2° (hydrophilic)
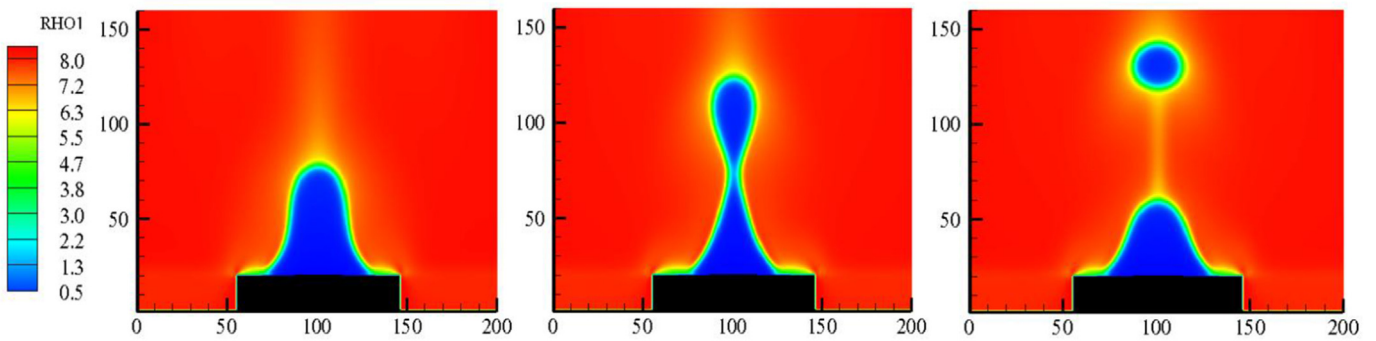
(b) Static contact angle of 123.3°(hydrophobic)

Fig. 12. Influence of contact angle on the bubble growth process.
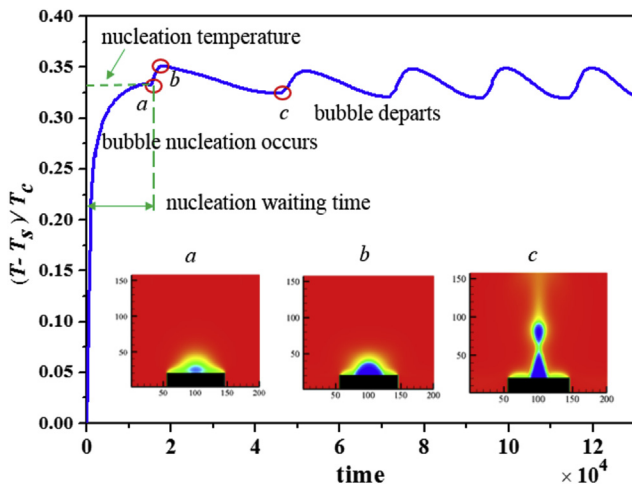
Fig. 13. Average wall temperature vs. time.
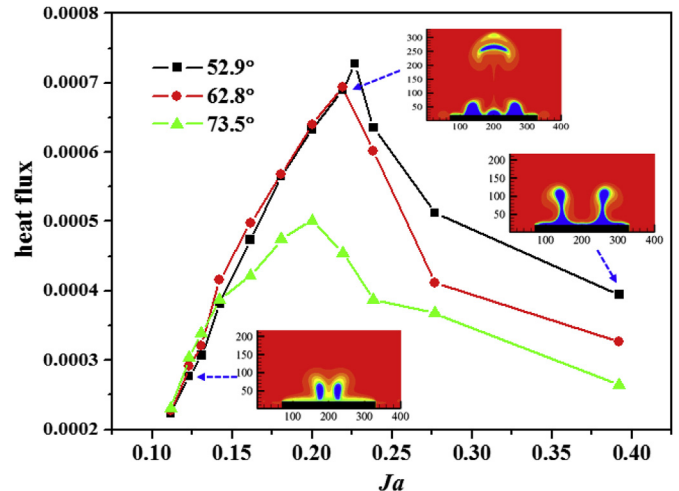
Fig. 14. Comparison of boiling curve.

Table 2
Nucleation waiting time of first bubble vs. static contact angle.

Static contact angle	38.2°	52.9°	89.9°	101.4°	113.2°	123.2°
Nucleation waiting time	47000	30000	15600	10600	7800	6300

vapor first occurs at the cavity and becomes the nucleus site of the bubble. After the bubble departure, the remained vapor trapped in

the cavity speeds up the bubble generation. Fig. 15(b) shows the comparisons of the local heat flux of surface with different cavity widths, which shows that there exists an optimal width of the rectangular cavity making the best heat transfer performance of the surface. In the present study, it is found that if the rectangular cavity width is larger than 20, the three-phase contact point occurs at upper corner of the cavity; while if the rectangular cavity width equals 10, the three-phase contact point expands along the surface (shown in the right bottom of Fig. 15 (a)). The position of three-

(a) Average heat flux of the surface   (b) Local heat flux
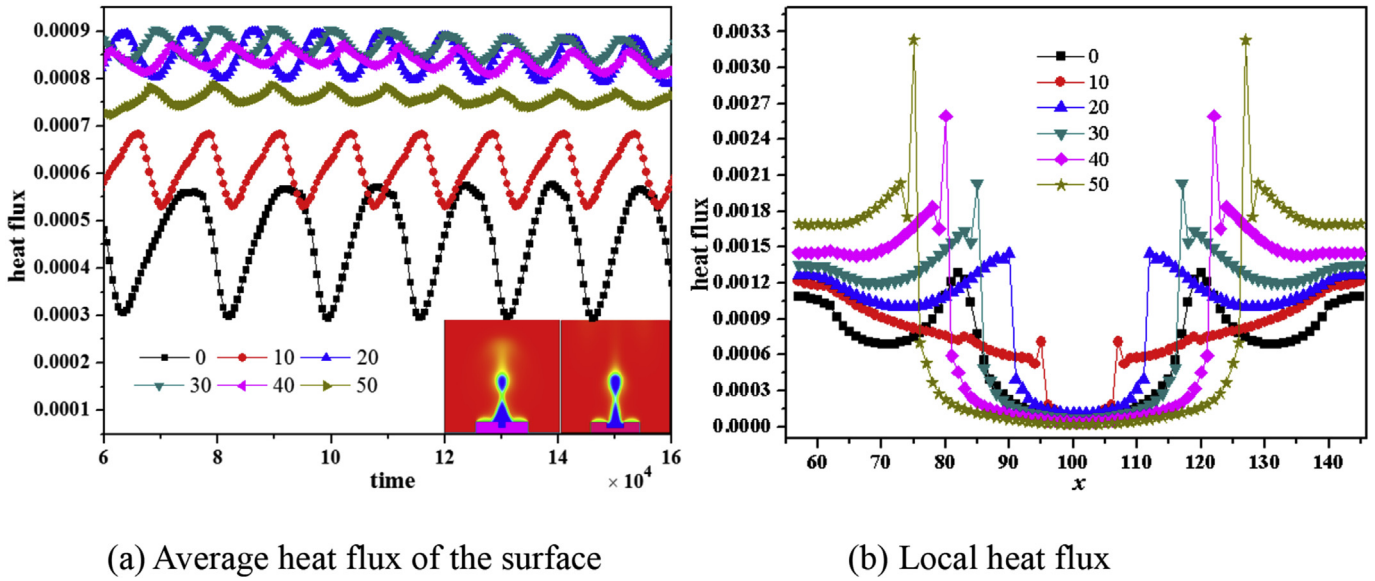
Fig. 15. Comparisons of heat flux of surfaces with different cavity widths.

phase contact point explains the maximum local heat flux occurring at the corner of the cavity. As shown in Fig. 15(b), the local heat flux of the surface covered by liquid increases with cavity width. This is because the rate of liquid-vapor phase change increases with the cavity width, and the liquid covering at the wetting surface will absorbs more latent heat (can be seen at the density contour adjacent to the wetting surface). However, the surface covered by the vapor has a rather low local heat flux. Therefore, there exists an optimal cavity width making the average wall heat flux highest.

3.5.2. Influence of cavity shape

Fig. 16 shows comparisons of the heat flux of different cavity shapes. The shapes of the cavity include circle, triangular, trapezium, and rectangular. The average heat flux and local heat flux of surfaces with different shapes of cavity are shown in Fig. 16(a) and Fig. 16(b), respectively.

It can be seen that the average heat flux of the roughened

surface with the cavity shape of circle has the best heat transfer performance; secondly is the triangular; and then is trapezium; finally is rectangular. The surface cavity is the nucleation site of the bubble and it may speed up the bubble departure frequency. Compared with the surface without cavity, the time-averaged heat fluxes are enhanced by 63%, 50%, 44%, 42% for circle, triangular, trapezium and rectangular, respectively. The detail local heat flux is shown in Fig. 16(b), which shows that for the most part of the circle surface, its local heat flux is the highest among five shapes. It agrees with the experimental work conducted by Das et al. [37] that the surface with circular groove performed the best.

4. Conclusions

In the present paper, a multiple-relaxation-time pseudopotential lattice Boltzmann model combined with a modified thermal lattice Boltzmann method is adopted to simulate the bubble

(a) Average heat flux of the surface   (b) Local heat flux
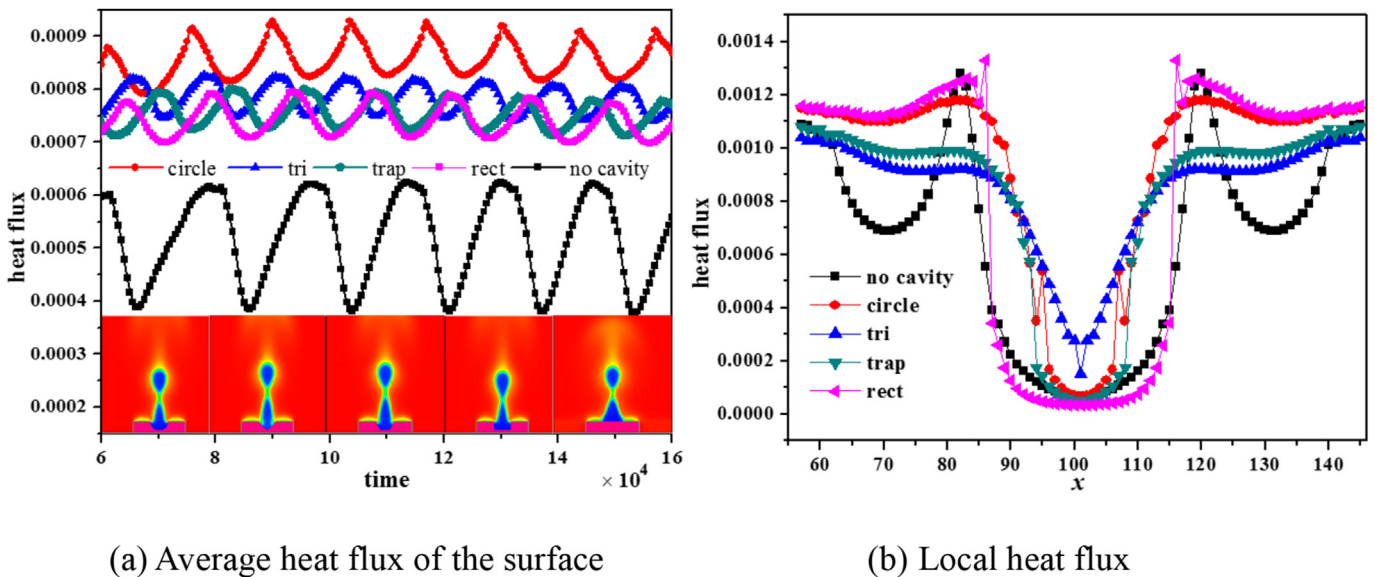
Fig. 16. Comparison of the heat flux of surfaces with different shapes of cavity.

nucleation, growth and departure process on a heated plate for two-dimensional situations. The modified phase-change pseudo-potential MRT LB model can approximately achieve thermodynamic consistency and a smaller value of a in P-R equation of state can reduce the spurious currents at the interface, which allows us to simulate the bubble nucleation at a large density ratio up to 200. The conjugated boundary of heated plate and fluids are properly dealt with to account for the rapid changes of ρc_v in the liquid-solid two domains. With the developed method, the boiling heat transfer performance at two saturation temperatures, $T_s = 0.68T_c$ and $0.86T_c$, are compared and the influences of surface wettability and cavities on the boiling heat transfer are investigated. Following conclusions can be made:

(1) The temperature of solid surface covered with vapor is higher than that covered with liquid; the boiling heat flux increases during the rewetting process while decreases during the bubble expansion process. The average heat flux of boiling at $T_s = 0.68T_c$ is much larger than that at $T_s = 0.86T_c$. The vapor bubble occurs earlier at $T_s = 0.86T_c$;

(2) For the rectangular cavity, the vapor first occurs at the cavity and becomes the nucleus site of the bubble; the remained vapor trapped in the cavity speeds up the bubble generation; the average heat flux first increases with the width of the cavity and then decreases, reaching a peak at certain width of the cavity;

(3) Bubble occurs earlier on a hydrophobic surface than a hydrophilic surface; for the hydrophilic surface, the surface is covered by liquid after bubble departure, while for the hydrophobic surface, a residual vapor is remained on the surface and can serve as the vapor embryo of the next bubble, thus resulting in no nucleation waiting time for the next bubble. In the simulated boiling curve, the maximum (critical) heat flux decreases with the decreasing wettability of the surface;

(4) For five different 2D shapes of cavity, at the same other conditions, the average heat flux of the circle cavity is the highest, and that of the plane surface is the lowest.

Acknowledgment

References

[1] Shojaeian M, Koşar A. Pool boiling and flow boiling on micro-and nano-structured surfaces. Eep Therm Fluid Sci 2015;63:45–73.

[2] Dong Z, Xu J, Jiang F, et al. Numerical study of vapor bubble effect on flow and heat transfer in microchannel. Int J Therm Sci 2012;54:22–32.

[3] Nam Y, Wu J, Warrier G, et al. Experimental and numerical study of single bubble dynamics on a hydrophobic surface. ASME J Heat Tran 2009;131:121004.

[4] Kreith F, Manglik RM, Bohn MS. Principles of Heat Transfer. seventh ed. Stamford, CT. USA: CENAGE Learning; 2011 [Chapter 10].

[5] Yang SM, Tao WQ. Heat Transfer. fourth ed. Beijing: Higher Education Press; 2006. Chapter Seven.

[6] Son G, Dhir VK. Numerical simulation of saturated film boiling on a horizontal surface. ASME ASME J Heat Tran 1997;119:525–33.

[7] Welch SWJ, Wilson J. A volume of fluid based method for fluid flows with phase change. J Comput Phys 2000;160:662–82.

[8] Sun DL, Tao WQ. A coupled volume-of-fluid and level set (VOSET) method for computing incompressible two-phase flows. Int J Heat Mass Tran 2010;53:645–55.

[9] Ling K, Li ZY, Tao WQ. A direct numerical simulation for nucleate boiling by the VOSET method. Numer Heat Tr A-Appl 2014;65:949–71.

[10] Shan X, Chen H. Lattice Boltzmann model for simulating flows with multiple phases and components. Phys Rev E 1993;47:1815.

[11] Chen L, Kang QJ, Mu YT, et al. A critical review of the pseudopotential multiphase lattice Boltzmann model: methods and applications. Int J Heat Mass Tran 2014;76:210–36.

[12] Chen L, Luan HB, He YL, et al. Pore-scale flow and mass transport in gas diffusion layer of proton exchange membrane fuel cell with interdigitated flow fields. Int J Therm Sci 2012;51:132–44.

[13] Hazi G, Markus A. On the bubble departure diameter and release frequency based on numerical simulation results. Int J Heat Mass Tran 2009;52:1472–80.

[14] Márkus A, Házi G. On pool boiling at microscale level: the effect of a cavity and heat conduction in the heated wall. Nucl Eng Des 2012;248:238–47.

[15] Gong S, Cheng P. Lattice Boltzmann simulation of periodic bubble nucleation, growth and departure from a heated surface in pool boiling. Int J Therm Sci 2013;64:122–32.

[16] Zhang C, Hong F, Cheng P. Simulation of liquid thin film evaporation and boiling on a heated hydrophilic microstructured surface by lattice Boltzmann method. Int J Heat Mass Tran 2015;86:629–38.

[17] Gong S, Cheng P. Numerical simulation of pool boiling heat transfer on smooth surfaces with mixed wettability by lattice Boltzmann method. Int J Heat Mass Transf 2015;80:206–16.

[18] Gong S, Cheng P. Two-dimensional mesoscale simulations of saturated pool boiling from rough surfaces. Part II: bubble interactions above multi-cavities. Int J Heat Mass Tran 2016;100:938–48.

[19] Li Q, Kang QJ, Francois MM, et al. Lattice Boltzmann modeling of boiling heat transfer: the boiling curve and the effects of wettability. Int J Heat Mass Tran 2015;85:787–96.

[20] Karani H, Huber C. Lattice Boltzmann formulation for conjugate heat transfer in heterogeneous media. Phys Rev E 2015;91(2):023304.

[21] Li Q, Luo KH, Li XJ. Forcing scheme in pseudopotential lattice Boltzmann model for multiphase flows. Phys Rev E 2012;86:016709.

[22] Li Q, Luo KH, Li XJ. Lattice Boltzmann modeling of multiphase flows at large density ratio with an improved pseudopotential model. Phys Rev E 2013;87:053301.

[23] Guo ZL, Zheng C. Analysis of lattice Boltzmann equation for microscale gas flows: relaxation times, boundary conditions and the Knudsen layer. Int J Comput Fluid D 2008;22:465–73.

[24] Yu Z, Fan LS. Multi-relaxation-time interaction-potential-based lattice Boltzmann model for two-phase flow. Phys Rev E 2010;82:046708.

[25] Yuan P, Schaefer L. Equations of state in a lattice Boltzmann model. Phys Fluids 2006;18:042101.

[26] Li Q, Luo KH, Kang QJ, et al. Contact angles in the pseudopotential lattice Boltzmann modeling of wetting. Phys Rev E 2014;90:053301.

[27] He YL, Wang Y, Li Q. Lattice Boltzmann method: theory and applications, Science. Beijing. 2009.

[28] Lou Q, Guo ZL, Shi BC. Evaluation of outflow boundary conditions for two-phase lattice Boltzmann equation. Phys Rev E 2013;87:063301.

[29] Zhang T, Shi BC, Guo ZL, et al. General bounce-back scheme for concentration boundary condition in the lattice-Boltzmann method. Phys Rev E 2012;85:016701.

[30] Tao WQ. Numerical Heat Transfer. second ed. Xi'an: Xi'an Jiaotong University Press; 2000.

[31] Li L, Chen C, Mei R, et al. Conjugate heat and mass transfer in the lattice Boltzmann equation method. Phys Rev E 2014;89:043308.

[32] Fritz W. Maximum volume of vapor bubbles. Phys Z 1935;36:379–84.

[33] Zuber N. Nucleate boiling. The region of isolated bubbles and the similarity with natural convection. Int J Heat Mass Tran 1963;6:53–78.

[34] Jo HJ, Ahn HS, Kang SH, et al. A study of nucleate boiling heat transfer on hydrophilic, hydrophobic and heterogeneous wetting surfaces. Int J Heat Mass Tran 2011;54:5643–52.

[35] Myers JG, Yerramilli VK, Hussey SW, et al. Time and space resolved wall temperature and heat flux measurements during nucleate boiling with constant heat flux boundary conditions. Int J Heat Mass Tran 2005;48:2429–42.

[36] Chen R, Lu MC, Srinivasan V, et al. Nanowires for enhanced boiling heat transfer. Nano Lett 2009;9:548–53.

[37] Das AK, Das PK, Saha P. Performance of different structured surfaces in nucleate pool boiling. Appl Therm Eng 2009;29:3643–53.